The DOI for this manuscript is doi: 10.1175/JCLI-D-11-00673.1

The final published version of this manuscript will replace the preliminary version at the above DOI once it is available.

If you would like to cite this EOR in a separate work, please use the following full citation:

Ummenhofer, C., F. Schwarzkopf, G. Meyers, E. Behrens, A. Biastoch, and C. Böning, 2012: Pacific Ocean Contribution to the Asymmetry in Eastern Indian Ocean Variability. J. Climate. doi:10.1175/JCLI-D-11-00673.1, in press.

Pacific Ocean Contribution to the Asymmetry in Eastern Indian Ocean Variability

Caroline C. Ummenhofer *

Climate Change Research Centre, University of New South Wales, Sydney, Australia

Franziska U. Schwarzkopf

Helmholtz Centre for Ocean Research Kiel (GEOMAR), Kiel, Germany

Gary Meyers

CSIRO Marine and Atmospheric Research, and Institute of Marine and Antarctic Research, University of Tasmania, Hobart, Australia

Erik Behrens, Arne Biastoch, Claus W. Böning

Helmholtz Centre for Ocean Research Kiel (GEOMAR), Kiel, Germany

*Corresponding author address: Caroline C. Ummenhofer, Climate Change Research Centre, University of New South Wales, Kensington, NSW 2052, Sydney, Australia.

E-mail: cummenhofer@whoi.edu

ABSTRACT

Variations in eastern Indian Ocean upper-ocean thermal properties are assessed for the period 1970–2004, with a particular focus on asymmetric features related to opposite phases of Indian Ocean Dipole events, using high-resolution ocean model hindcasts. Sensitivity experiments, where interannual atmospheric forcing variability is restricted to the Indian or Pacific Ocean only, support the interpretation of forcing mechanisms for large-scale asymmetric behavior in eastern Indian Ocean variability. Years are classified according to eastern Indian Ocean subsurface heat content (HC) as proxy of thermocline variations. Years characterized by anomalous low HC feature a zonal gradient in upper-ocean properties near the equator, while high events have a meridional gradient from the tropics into the subtropics. The spatial and temporal characteristics of the seasonal evolution of HC anomalies for the two cases is distinct, as is the relative contribution from Indian Ocean atmospheric forcing versus remote influences from Pacific wind forcing: low events develop rapidly during austral winter/spring in response to Indian Ocean wind forcing associated with an enhanced southeasterly monsoon driving coastal upwelling and a shoaling thermocline in the east; in contrast, formation of anomalous high eastern Indian Ocean HC is more gradual, with anomalies earlier in the year expanding from the Indonesian Throughflow (ITF) region, initiated by remote Pacific wind forcing and transmitted through the ITF via coastal wave dynamics. Implications for seasonal predictions arise with high HC events offering extended lead times for predicting thermocline variations and upper-ocean properties across the eastern Indian Ocean.

1. Introduction

Recent work has demonstrated the importance of eastern Indian Ocean variability for regional rainfall and drought for Australia (Ummenhofer et al. 2008, 2009b), Indonesia (Hendon 2003), and more widely across southeast Asia (e.g., Sinha et al. 2011). Given the slower evolution of anomalies in the ocean, as opposed to the higher frequency variability of the atmosphere, and the associated benefits for seasonal predictions, an improved understanding of the drivers of eastern Indian Ocean variability and its evolution is desirable. Here, using high resolution ocean model hindcasts, we investigate Indo-Pacific upper-ocean properties to quantify the contributions of local and remote forcing factors to characteristic features in interannual variations across the eastern Indian Ocean and how they might benefit seasonal predictions.

In contrast to the eastern equatorial Pacific and Atlantic Ocean with their prevailing easterly trades, favoring a Bjerknes feedback with shallow thermocline and enhanced upwelling, the annual mean thermocline in the eastern Indian Ocean is flat with little upwelling occurring (Schott et al. 2009). Despite this suggesting an absence of the Bjerknes feedback in the Indian Ocean, the strong seasonal variability of the monsoon winds leads to a narrow window during austral winter and spring that supports a Bjerknes feedback and the development of Indian Ocean Dipole (IOD; Saji et al. 1999; Webster et al. 1999) events. The IOD is therefore strongly phase-locked to the seasonal cycle, developing in June, peaking in October and rapidly terminating thereafter with the reversal of the monsoon winds. Anomalous atmospheric forcing across the Indo-Pacific region associated with the El Niño-Southern Oscillation (ENSO) clearly plays a large role in modulating eastern Indian Ocean variability on interannual timescales, often leading to the coincidence of ENSO and IOD events. Using a conceptual coupled five-box model, Li et al. (2003) identified ENSO as a trigger for IOD development, though not all observed IOD events of the last 50 years could thus be reproduced, indicating that other factors were at play during the positive IOD events of 1961 and 1994. Apart from ENSO, Fischer et al. (2005) found unseasonably early strengthening of the southeasterly trades over the eastern Indian Ocean to trigger IOD events.

Many previous studies largely focus on local air-sea interaction, either arising from variability inherent to the Indian Ocean or via the atmospheric bridge forced by ENSO, acting on upper-ocean properties in the Indian Ocean. However, what is the role of oceanic preconditioning in the eastern Indian Ocean, either inherent to the region or due to remote Indo-Pacific forcing? The timescale for the local air-sea interactions is seasonal to interannual, while the oceanic preconditioning and/or an oceanic bridge act on longer timescales that might be useful for improved predictions. Using ocean model experiments, Annamalai et al. (2005) showed the background state of the eastern equatorial thermocline to be important for the development of IOD events: with a shallow background state of the eastern Indian Ocean thermocline, owing largely to Pacific decadal variability, strong IOD events can occur more frequently even in the absence of strong atmospheric forcing associated with El Niño; in contrast, during periods with a deep thermocline in the Indian Ocean, strong El Niño-related wind forcing over the Indonesian archipelago is required to trigger an IOD event. According to Annamalai et al. (2005), the background state of the eastern Indian Ocean thermocline over the past 50 years could help to explain decadal modulation in the frequency of IOD events and variations in their (in)dependence from ENSO. Here, we hope to explore the role of remote Pacific forcing for preconditioning of the eastern Indian Ocean thermocline on interannual timescales. The focus is on the role of Pacific winds and their transmission to the eastern Indian Ocean through the oceanic bridge, which we will investigate using ocean general circulation model (OGCM) experiments forced with various wind field configurations.

Tropical Indian Ocean variability exhibits a distinct asymmetry between opposite phases of the IOD during its mature phase in austral spring (September–November (SON); Hong et al. 2008a,b): anomalies during positive IOD events are relatively stronger than during negative IOD events, as seen for SST (Fig. 1): the zonal SST gradient across the tropical Indian Ocean exhibits larger deviations from its mean state during positive IOD events, than during negative ones; this is mostly owed to larger anomalies in the eastern equatorial Indian Ocean during positive IOD events, while the magnitude of anomalies in the west is comparable during opposite phases of the IOD. The asymmetry is not limited to the surface ocean, but also manifests itself in precipitation and atmospheric circulation over the region and is intricately linked to the IOD evolution (Wu et al. 2008).

According to Hong et al. (2008a) the negative SST skewness in the eastern Indian Ocean can largely be attributed to asymmetric local air-sea feedbacks (cf. Fig. 1). They found the nature of the wind stress-ocean advection-SST feedback to be the major cause of the asymmetry. In contrast, Zheng et al. (2010) propose that an asymmetric SST-thermocline feedback (cf. Fig. 1) is responsible for the observed asymmetry in the equatorial Indian Ocean: i.e. that due to the relatively deep thermocline in the eastern Indian Ocean, a shoaling thermocline can reduce subsurface ocean temperatures significantly (Fig. 1a), while a deepening of the thermocline will have less of an effect on SST (Fig. 1b).

The present study will expand on this previous body of work by exploring the role of remote forcing from the Pacific Ocean for the observed asymmetry in eastern Indian Ocean variability. Furthermore, our assessment of asymmetric eastern Indian Ocean variability here will broaden the scope beyond the immediate area of the tropical eastern pole of the IOD (90°–110°E, 0–10°S) that has been previously investigated (cf. Hong et al. 2008a,b; Zheng et al. 2010): i.e. our study of eastern Indian Ocean variability will encompass the eastern half of the Indian Ocean, including the subtropical southeastern Indian Ocean and northwest shelf off Australia, both areas found to be important in modulating the regional atmospheric circulation and Australian rainfall (Ummenhofer et al. 2008, 2009b). As can be seen from Fig. 1, the SST during positive and negative IOD events shows distinct anomaly patterns: positive IOD events are characterized predominantly by a zonal SST gradient across the equatorial Indian Ocean (Fig. 1a), while the negative IOD has a meridional gradient from the warm tropics to the cool subtropics (Fig. 1b). The asymmetry between zonal and meridional gradients in opposite phases of the IOD is the focus of the present study, with a particular emphasis on the contribution from remote Pacific forcing for this. Upper-ocean thermal properties across the eastern Indian Ocean, especially over the northwest shelf off Australia, can play a large role in regional climate, for example for Australian rainfall (Ummenhofer et al. 2008, 2009b), Leeuwin Current strength (Hendon and Wang 2010) and ultimately for management of the marine environment off Western Australia.

The eastern Indian Ocean is a highly dynamical region characterized by complex interactions of factors: the Indonesian Throughflow (ITF) region surrounding the Indonesian archipelago represents the intersection of equatorial wave guides from the Indian and Pacific Oceans (Wijffels and Meyers 2004). As such, remote influences from both ocean basins contribute to the region's variability, as well as local ocean-atmosphere interactions. Variations in eastern Indian Ocean thermocline depth, of considerable importance for IOD development (e.g., Annamalai et al. 2005), can be directly forced by local winds, but they can also be influenced by remote forcing propagated via baroclinic waves (Schott et al. 2009).

It is well-known that signals from remote Pacific wind forcing penetrate through the ITF region and cause sea level and thermocline depth variations along the coastline of Western Australia, often varying in phase with ENSO events (Meyers 1996; Wijffels and Meyers 2004). This is consistent with theoretical considerations by Clarke and Liu (1994), who used coastal dynamics to link tropical Pacific variability to variations in northwest Australian sea level records and interannual variability in ITF transport (Clarke and Liu 1994; Meyers 1996): the remote signal, initiated in the central Pacific by zonal wind anomalies, is transmitted by westward propagating Rossby waves in the Pacific, becoming coastally-trapped waves at the intersection of the equator and New Guinea (Wijffels and Meyers 2004). They travel poleward along the Australian coastline and radiate Rossby waves into the southern Indian Ocean (Cai et al. 2005). The strength of the transmission of the remote signal from the Pacific to the Indian Ocean varies on multidecadal timescales (Shi et al. 2007), with variations in Pacific wind stress thus reflected in eastern Indian Ocean heat content and sea level anomalies (Schwarzkopf and Böning 2011), ITF and Leeuwin Current transport (Feng et al. 2011).

In light of observed recent changes across the Indo-Pacific, it is important to explore the relative roles of local and remote Pacific forcing for variability across the wider eastern Indian Ocean region on interannual to longer timescales. The Indian Ocean has sustained considerable upper-level warming, particularly in the subtropics, accompanied by a subsurface cooling in the tropical eastern Indian Ocean (Alory et al. 2007), and a shoaling of the off-equatorial thermocline in the southeastern Indian Ocean (Cai et al. 2008), with most of these trends related to trends in the equatorial Pacific. Recent changes in the thermocline depth are not limited to the Indian Ocean, but have also been reported for the Pacific Ocean (e.g., Williams and Grottoli 2010; Collins et al. 2010). The close interaction between the two ocean basins, along with robust changes observed and projected for Indo-Pacific climate, further necessitate an improved understanding of eastern Indian Ocean variability.

The remainder of the paper is structured as follows: Section 2 describes the observational data sets and ocean model simulations. In Section 3, the model's representation of Indo-Pacific variability is compared to observations. Asymmetry in eastern Indian Ocean variability is explored in Section 4, followed by an assessment of the role of remote forcing from the Pacific for this asymmetry (Section 5). Section 6 presents the propagation and seasonal evolution of the remote signal, with implications for predicting eastern Indian Ocean variability (Section 7). Our main findings are summarized in Section 8.

2. Data sets and ocean models

The ocean model's representation of upper-ocean properties is assessed against observational products across the Indo-Pacific region. The comparison focuses on the overlapping period between the observational product and the ocean model hindcasts for the analysis period 1970–2004. We used the monthly HadISST product (Rayner et al. 2003) by the UK Met Office, Hadley Centre for Climate Research, at 1° spatial resolution for the period 1970–2004. For monthly sea surface height (SSH), the merged product of gridded mean sea level anomalies, as provided by Ssalto/Duacs through Aviso, was employed for the period 1993–2004.

a. *Ocean model simulations*

A series of global ocean model simulations at different horizontal resolutions were analyzed (Table 1). They all build on the ocean/sea-ice numerical Nucleus for European Modelling of the Ocean (NEMO) framework (Madec 2007). The control (CTRL) is a global hindcast simulation with the OGCM ORCA at 0.5° horizontal resolution forced with atmospheric forcing for the period 1958–2004, following a 20-yr spin-up phase. The atmospheric forcing fields are those of the Coordinated Ocean Reference Experiments (CORE; Griffies et al. 2009), building on the refined reanalysis products of Large and Yeager (2004), who combined reanalysis fields by the National Center for Environmental Prediction (NCEP) and National Center for Atmospheric Research (NCAR) fields with satellite and other observations to correct for biases and global imbalances. In the simulations, we used bulk formulae that work with atmospheric forcing data at synoptic timescale and very weak sea surface salinity restoring with a 1-year timescale. Both aspects are of particular importance in the context of this study for an almost free evolution of surface quantities. To further ascertain that results are independent of model resolution a comparable hindcast simulation at 0.25° horizontal resolution (CTRL_0.25) was conducted (Section 6). To identify and correct for spurious model drift, the simulations at both 0.5° and 0.25° resolution were repeated with global climatological (the "normal year" CORE product) forcing. From all interannually forced simulations, linear trends for the period 1970–2004 in the respective climatological simulation (CLM and CLM_0.25) were subtracted.

In addition to the control simulations, a set of perturbation experiments were conducted (for details see Table 1). In these experiments, interannual atmospheric forcing was restricted to an ocean basin only, while climatological forcing was employed elsewhere. Here, we present results for the Pacific Ocean and Indian Ocean experiments at 0.5° horizontal resolution, with the respective masks used in the experiments indicated in Fig. 2. To avoid spurious instabilities in the simulations at the edge of the masks, linear damping was employed to interpolate between climatological and interannual forcing over a 5° latitude/longitude band. The following set of experiments used global climatological forcing, plus interannual forcing of heat fluxes and wind stress in the Pacific Ocean only (PO_{HF+WS}), and in the Indian Ocean only (IO_{HF+WS}). Furthermore, experiments were conducted with interannual forcing of both wind stress and heat fluxes in one of the ocean basins, while interannual forcing was restricted to heat fluxes elsewhere ($PO_{HF}IO_{HF+WS}$ and $PO_{HF+WS}IO_{HF}$). A summary of all the experiments used here is given in Table 1 and further details also provided in Schwarzkopf and Böning (2011).

3. Model evaluation

The comparison of the model's representation of upper ocean properties in the Indo-Pacific region with observations is illustrated with SSH fields in Fig. 3. SSH is chosen as it integrates properties in the upper ocean and can be understood as a proxy for variations in the thermocline depth (Hong and Li 2010). A good representation of the latter in the model is particularly relevant in the context of this study. In Fig. 3, the seasonal deviation from the long-term mean SSH, along with its seasonal standard deviation (SD), are compared between observations and the CTRL simulation. Focus is on the June–August (JJA) and SON seasons, when variations in eastern Indian Ocean properties are strongest (Fig. 3e–h).

During JJA, much of the eastern and equatorial Indian Ocean is characterized by positive SSH anomalies up to 0.2m in an area extending from the southwestern tip of Australia to Sumatra, covering the entire northwest shelf off Australia and in a band westward along the equator between 10°S and 10°N (Fig. 3a,b). The western Pacific (5°–20°N) also shows positive SSH anomalies, extending eastward at around 15°N. Negative SSH anomalies are seen in the Indonesian Seas, central subtropical Indian Ocean, and north of Madagascar. The overall pattern is well reproduced by the model, though the magnitudes in SSH are slightly underestimated. In SON, negative SSH anomalies, indicative of a shoaling thermocline, occur off the Sumatra and Java coastlines (Fig. 3c,d). The upwelling along the Indonesian coastline is driven by the seasonally strengthening southeasterly winds. In the central subtropical Indian Ocean (5°–20°S), an area of positive SSH anomalies is seen, indicative of Rossby waves associated with wind stress variations off Sumatra (Li et al. 2002). The model captures the broad patterns of SSH anomalies across the Indo-Pacific, in particular the propagation of Rossby waves and coastal upwelling, though the magnitude of the upwelling-associated negative anomalies is overestimated during SON.

In addition to the representation of the mean seasonal cycle, SSH variance is of interest as well (Fig. 3e–h). The observed SD of SSH during JJA is largest in the vicinity of western boundary currents, such as the East Australian Current and the Agulhas region, as well as the Leeuwin Current (Fig. 3e). The variations in the model in these regions are of reduced magnitude (Fig. 3f), most likely related to model resolution, as the same model at higher resolution reproduces features of these currents well (e.g., Feng et al. 2008). The model underestimates SSH variability in the central subtropical Indian Ocean and south of Australia. In the model, regions of increased variability during JJA, and even more so during SON, include the western Pacific (5°-15°N, 125°-150°E), the coastal upwelling region along Sumatra, and a band across the south equatorial Indian Ocean (10°-20°S). These areas all match well with the observed during both seasons. Good representation of the model in these regions in the eastern Indian Ocean and western Pacific in particular are of main concern here and highlight the model's utility for the present study.

Temporal variations in SST and SSH in the model compared to observations are shown for a time-series in the eastern Indian Ocean in Fig. 4. The box used for the spatial average is delimited by 90°–110°E and 0–10°S, only contains the area west of Sumatra (cf. box in Fig. 3h), and will be referred to as "eIO" region in the remainder of the study. It encloses the region along the Sumatran coastline characterized by upwelling during the second half of the year. For the time-series, anomalies from the monthly climatology were created and normalized by dividing by the SD to facilitate comparison between variables and between observations and model. Fig. 4 represents the 6-month running mean of this normalized anomaly time-series for the three variables.

The 6-month running mean time-series of standardized SST show close agreement between model and observations over the analysis period 1970–2004 (Fig. 4a). Strong positive IOD events, such as in 1982, 1994, and 1997, are captured by the model. The amplitudes during IOD events are slightly overestimated, which could be related to biases in the upwelling near the coast. Overall, the variability between the two eIO SST time-series compares well and they are significantly correlated with a Pearson correlation coefficient of 0.71 ($P<0.001$). The model-observed intercomparison of SSH variability in the eIO region can only be conducted over the period 1993–2004, when remotely-sensed SSH is available from Aviso. Over this common period, model and observed SSH are significantly correlated with a correlation coefficient of 0.86 (P<0.001). Again, the positive IOD events in 1994 and 1997 are clearly seen in the SSH signal of model and observed (Fig. 4b).

In addition to SSH, also shown is subsurface heat content, vertically integrated between 50 and 320 m, which we use here as proxy for variations in the thermocline. The good agreement between SSH, heat content, and SST in the CTRL simulation (all significantly correlated at the 99% level; Fig. 4) indicates that heat content is representative of upper ocean variability, associated with changes in the thermocline, and is linked to surface properties at the ocean-atmosphere interface. In this study, the advantage of using subsurface heat content is that it is not directly tied to the local surface atmospheric forcing. That way, anomalies forced remotely in the perturbation experiments can still be seen in subsurface variations, while SST only reflects local (climatological) forcing by surface fluxes and winds. In other words, in the perturbation experiments, using subsurface heat content allows us to distinguish between effects initiated by atmospheric forcing inherent to the Indian Ocean and remote Pacific effects transmitted through the ocean. A similar approach has been employed in previous modeling studies (e.g., Schwarzkopf and Böning 2011).

4. Asymmetry in eastern Indian Ocean variability

It is well-known that the eastern pole of the IOD is characterized by a distinct asymmetry between positive and negative events, as described in previous studies (e.g., Hong et al. 2008a,b; Zheng et al. 2010). This asymmetry is apparent in the relationship between eIO SST anomalies and heat content anomalies in Fig. 5. The scatterplot, as well as the following analyses, focus on the SON season, when interannual variations in the eastern Indian

Ocean are largest. The magnitudes of anomalies in SST and heat content during negative events are enhanced by approximately 50% compared to positive events: 1994 and 1997 are characterized by negative anomalies of almost 1.2°C and approximately 300°C m in heat content, while anomalies during positive events only reach approximately 0.4°C and 160°C m (Fig. 5). Such asymmetric behavior in eastern Indian Ocean variability, as manifest in the magnitude of IOD events, has previously been linked to asymmetries in the strength of the thermocline feedback (Zheng et al. 2010) and asymmetric ocean-atmosphere feedbacks (Hong and Li 2010) over the eastern Indian Ocean. Here, the asymmetry in eIO variability is investigated further, with a focus on linking these locally asymmetric features to changes in the larger eastern Indian Ocean region and beyond using composite analysis.

For this purpose, we defined events with anomalous low and high eIO heat content during SON. In the definition of these events, the nonlinear nature of eIO variability needs to be taken into account. This renders a criterion-based approach, such as choosing those events exceeding ±1 SD of SST or heat content, unsuitable. Instead, all 35 years of the analysis period (1970–2004) were ranked according to their eIO heat content during SON and divided into quintiles of seven members each. Low heat content events were taken as those in the lowest quintile, high heat content events as those in the uppermost quintile, highlighted as blue and red circles in Fig. 5, respectively. Such an approach is customary when assessing events for variables with a nonlinear, skewed distribution, such as precipitation or drought. To ascertain the robustness of the results, in addition to using seven high/low heat content years, the analyses were repeated using five and nine years each as well. Furthermore, ranking according to SST, rather than heat content, was employed as well. Results overall remained robust with these varying definitions. Therefore, in line with previous advantages of using subsurface heat content (cf. Section 3) over SST, further composite analyses are only presented for high/low events based on quintiles of eIO heat content during SON.

Composites of a range of regional anomaly fields during years with low and high eIO heat content anomalies are shown in Fig. 6. To further highlight asymmetries the sum of composite anomalies during events with high and low heat content anomalies are provided in Fig. 7. Zonal wind stress anomalies indicate strengthened easterly flow around the Indonesian archipelago and over the northern Indian Ocean (5°S–20°N) during SON of low heat content events (Fig. 6a). In contrast, high heat content anomaly years are characterized by weakened easterly flow during SON over the eastern Indian Ocean (5°S–15°N, 70°–110°E; Fig. 6b). Over the western Pacific (0°–15°N), significant zonal wind anomalies of opposite sign to the Indian Ocean signal are apparent (Fig. 6a,b), which are enhanced east of 160°E during high events, compared to low events (Fig. 7a).

In line with a strengthened southeasterly monsoon, composite SST anomalies during low heat content events show cooler temperatures in the tropical eastern Indian Ocean and around the Indonesian archipelago (Fig. 6c). Cooler temperatures are also seen in the western tropical Pacific, while the tropical western Indian Ocean is anomalously warm. During high heat content events, warm SST anomalies in the tropical eastern Indian Ocean are locally more constrained to the immediate upwelling region along the Sumatra and Java coastlines and the Indonesian archipelago (Fig. 6d). Anomalous cool SST dominate across the entire western half and subtropical Indian Ocean. Overall, the SST anomalies during low heat content events are reminiscent of the zonal SST gradient across the equatorial Indian Ocean during IOD events (Saji et al. 1999; Webster et al. 1999). In contrast, more extensive SST anomalies during high heat content events also feature a meridional gradient over the eastern Indian Ocean, previously shown to be of importance for modulating Australian rainfall (Ummenhofer et al. 2008, 2009b). This asymmetry in the SST gradients between high and low events is also seen in Fig. 7b. However, the asymmetries in zonal wind stress between low and high heat content events do not closely match those in SST: considerable asymmetries exist in the zonal wind stress across the central and western tropical and subtropical Indian Ocean (Fig. 7a); on the other hand, the sum of SST anomalies indicates largest asymmetries in an area closely confined to the upwelling region off the coast of Sumatra and in the central subtropical Indian Ocean (Fig. 7b).

Anomalies in mixed layer depth (MLD; water with differences in potential density of less than 0.01 kg m^{-3} is defined as being part of the mixed layer) during low heat content events show reductions along the coastline of Sumatra and Java and locally in the northern and subtropical southern Indian Ocean. An area of increased MLD dominates in the central equatorial Indian Ocean 0°–15°S, 70°–110°E (Fig. 6e), indicative of downwelling Rossby waves, set up by the wind stress off Sumatra and propagating the anomalous signal westward (Li et al. 2002). During high heat content years, the anomalies along the Sumatra and Java coastlines indicate a deeper MLD (Fig. 6f). The asymmetry between opposite eIO phases in MLD is largest in the subtropical Indian Ocean at 20°–40°S, 70°–100°E (Fig. 7c).

Composites of SSH anomalies during low heat content events reveal an extensive area of reduced SSH across the eastern Indian Ocean, extending from the southwestern tip of Western Australia along the Leeuwin Current region, the northwest shelf off Australia, along Java and Sumatra and into the Bay of Bengal (Fig. 6g). The Indonesian archipelago and large parts of the western Pacific (5°S–20°N, 130°–170°E) are also dominated by decreased SSH, while positive SSH anomalies occur over the western and central Indian Ocean. High heat content events are characterized by extensive positive SSH anomalies across the eastern Indian Ocean and the western Pacific (Fig. 6h), with the spatial extent comparable to the low events. In the subtropics, high content events show low SSH extending from 20°S, 80°E southeastward towards Australia. The low contributes to the meridional aspect of anomalies in the high heat content case discussed before, compared to the zonal gradient seen in the low heat content events. The asymmetry becomes even more apparent in heat content (Fig. 6i,j, 7e): a clear meridional gradient in heat content anomalies is seen across the eastern tropical and subtropical Indian Ocean for high heat content events (Fig. 6j), while the signal in the low heat content events is mostly limited to the tropics (Fig. 6i). The low heat content events show some significant anomalies on the northwest shelf off Australia and a very thin coastal strip along the path of the Leeuwin Current, but the extent of the anomalies appears coastally trapped compared to the more widespread anomalies extending west towards 100°E in the southern Indian Ocean for high events (cf. Fig. 6i,j). In particular this signal extending from the northwest shelf of Australia towards East Africa along 10°–20°S is clearly seen in Fig. 7e. The western Pacific warm pool region also indicates a large asymmetry in heat content, with larger anomalies in high heat content events compared to low events (Fig. 7e).

To summarize, we investigate the well-known asymmetry in the magnitude of anomalies in eIO variability (e.g., Hong and Li 2010; Zheng et al. 2010) using composites of high and low heat content events. They reveal marked differences in the broad features of the anomalies across the eastern Indian Ocean between the two events, not limited to the eIO region that has so far been the focus of previous studies. Furthermore, the spatial extent and magnitude of anomalies across the western Pacific Ocean differ markedly between the two cases. It is therefore of interest to further explore the contribution of remote forcing from the Pacific to the asymmetry seen in thermocline variations across the eastern Indian Ocean.

5. Indian Ocean forcing versus remote Pacific impacts

To separate the effects of local and remote atmospheric forcing on upper-ocean variability across the eastern Indian Ocean, a series of sensitivity experiments were conducted (cf. Section 2a; Table 1). Composite heat content anomalies are shown in Fig. 8 for the simulations with full interannual atmospheric forcing restricted to the Indian or Pacific Ocean, respectively (while climatological forcing is employed elsewhere). The years chosen as low and high heat content events for the composite are based on the CTRL simulation (cf. Fig. 5). In Fig. 8, we compare the heat content anomalies during low/high events in the CTRL simulation (Fig. 6i,j) with those in the sensitivity experiments to distinguish effects of interannual atmospheric forcing in a particular ocean basin only from those of the global interannual forcing.

Using full interannual atmospheric forcing over the Indian Ocean only (IO_{HF+WS} experiment), the heat content anomalies during low events very closely resemble the anomalies seen in the CTRL simulation north of about 17°S, except in the region off the coast of Western Australia (cf. Figs. 8a, 6i). The coastal Leeuwin Current shows reduced heat content anomalies in the CTRL, which is not reproduced in the IO_{HF+WS} simulation. The similarity in pattern and magnitude of the tropical heat content anomalies between the two simulations indicates that tropical Indian Ocean upper-ocean variability during low heat content events is primarily driven by atmospheric forcing over the Indian Ocean region. This is in agreement with Rao et al. (2002), who found a subsurface dipole signal in the tropical Indian Ocean to be predominantly forced by zonal winds in the equatorial region. During high heat content events, increased heat content is seen along Java and Sumatra, and extending into the Bay of Bengal; negative heat content anomalies occur in the central Indian Ocean (0°–15°S, 60°–80°E; Fig. 8b). Overall, the high heat content anomaly pattern resembles a mirror image of the low event case. This is in contrast to the heat content anomalies seen in the CTRL simulation during high heat content events (Fig. 6j). The entire signal with increased heat content off the coast of Western Australia is missing in the IO_{HF+WS} simulation, extending from Timor via the northwest shelf off Australia towards the southwestern tip of Western Australia. Also, the low heat content anomaly in the subtropics of the central Indian Ocean south of 25°S is missing (Fig. 8b), which is an important component of the meridional SST gradient seen in Fig. 6j.

In the PO_{HF+WS} experiment in the low heat content events, negative anomalies are present extensively across the western Pacific and much weaker in the eastern part of the Indonesian archipelago and off the coast of the Australian northwest shelf (Fig. 8c). However, no discernible heat content anomalies are seen in the tropical Indian Ocean north of Timor during low heat content events (Fig. 8c), confirming that it is regional Indian Ocean atmospheric forcing that generates Indian Ocean heat content anomalies during the low events. The high heat content events are characterized by extensive positive anomalies in the Leeuwin Current region and the northwest shelf off Australia extending towards Timor and radiating into the central Indian Ocean (Fig. 8d). They also exhibit enhanced heat content anomalies across the western Pacific and around the Indonesian archipelago. It is of interest to note that despite a comparable extent and magnitude of the heat content anomalies in the western Pacific between the two cases, only in the high heat content case does the signal develop in the region off Western Australia. This is further explored in Sections 6–7.

To further distinguish the respective roles of atmospheric forcing over the Indian and Pacific Ocean, two sets of experiments are used with full interannual forcing in either the Pacific or the Indian Ocean, while the rest of the global ocean experiences interannually varying heat fluxes, but climatologically fixed winds (cf. Table 1). In the PO_{HF} IO_{HF+WS} experiment (Fig. 8e,f), the absence of extensive heat content anomalies in the western Pacific during low and high heat content events indicates that these anomalies are driven by Pacific winds. Therefore they are present in Fig. 8g,h, which contains full interannual Pacific forcing. The lack of significant heat content anomalies in Fig. 8g with fully interannual forcing over the Pacific and Indian Ocean heat fluxes only, implies that heat content anomalies during low events are primarily driven by Indian Ocean winds (Rao et al. 2002), consistent with the Bjerknes feedback.

During high heat content events, tropical Indian Ocean heat content anomalies north of 10°S are also forced primarily by Indian Ocean winds. This is apparent from a signal present in the tropical Indian Ocean when forcing with fully interannual forcing in the Indian Ocean (PO_{HF} IO_{HF+WS} experiment; Fig. 8f), but absent when globally using interannual heat fluxes, in conjunction with fully interannual forcing in the Pacific (PO_{HF+WS} IO_{HF} experiment; Fig. 8h). The subtropical component of the positive heat content anomalies over the northwest shelf off Australia and the Leeuwin Current region appears to be a response to interannual Pacific Ocean winds, as it is absent in PO_{HF} IO_{HF+WS} (Fig. 8f,h). In contrast, the reduced heat content anomalies over the central subtropical Indian Ocean south of 20°S seem to be partly driven by Indian Ocean heat fluxes, consistent with heat budget analysis by Santoso et al. (2010). The more extensive negative anomalies in the subtropical Indian Ocean (Fig. 8f,b) also imply some role of interannual Pacific heat fluxes. However, some effects at the edge of the Indian Ocean mask cannot be excluded.

6. Propagation of the remote signal

a. Evolution of regional heat content anomalies

Given that the results so far imply that remote forcing by Pacific winds seems to impact eastern Indian Ocean heat content anomalies, at least during high heat content events, it is of interest to explore their seasonal evolution across the Indo-Pacific region. Fig. 9 shows the evolution of heat content anomalies as 3-month composites during years chosen as low/high events, plus during the three months leading into and out of the year. Given the analysis period of 1970–2004 in the model simulations, the high eIO heat content event of 1970 and the low event of 2004 had to be excluded from this composite.

During low heat content events, significant reductions appear along Sumatra and Java by June (Fig. 9e), associated with enhanced coastal upwelling driven by a strengthened southeasterly monsoon over the eastern Indian Ocean, as during positive IOD events (Saji et al. 1999; Webster et al. 1999). Over the following months, the negative anomalies increase in magnitude and spatial extent over the eastern Indian Ocean, including the northwest shelf off Australia and the Leeuwin Current region. Positive heat content anomalies in the central subtropical and western Indian Ocean develop rapidly from October onwards (Fig. 9i). Simultaneous with the evolution of the Indian Ocean heat content anomalies, negative anomalies also build up in the western Pacific (0°–20°N, 120°–160°E) from July onwards to cover much of the western half of the Pacific by December.

In high eIO heat content events, positive anomalies occur much earlier in the year across the eastern Indian Ocean, including the Leeuwin Current region, the Indonesian archipelago and the western Pacific (Fig. 9). Over the following months, the positive anomalies in the western Pacific intensify in magnitude and spatial extent. The region of significantly enhanced anomalies in the eastern Indian Ocean also expands from the northwest shelf towards Java/Sumatra and southwards along the Australian continent to cover much of the eastern half of the Indian Ocean by December.

Asymmetry in the temporal evolution of the heat content anomalies is apparent from Fig. 9: anomalies in the low events develop rapidly in the second half of the year from July onwards (Fig. 9g); in contrast during high events, the build-up of positive anomalies particularly off Western Australia is much slower, but progresses from the start of the year already (Fig. 9b). What is the reason for the asymmetry in the propagation of the remote signal from the Pacific to the Indian Ocean that leads to the differences in the spatial anomaly pattern across the eastern Indian Ocean recorded during low/high eIO heat content events? What factors determine that the transmission of the heat content anomalies from the Pacific to the Indian Ocean occurs during high heat content, but not during low events?

Focusing on the heat content anomalies in the Western Pacific, positive anomalies are already present for a high event at the end of the preceding year (Fig. 9b); however, significant anomalies there do not appear until July–September in the low event case. Extensive significant anomalies of heat content on the northwest shelf off Australia first occur $\sim$6 months after their appearance in the western Pacific, accounting for a signal on the northwest shelf in April–June (yr) in the high heat content event, but not until January–March (yr+1) in the year following a low event (Fig. 9f,k). This is likely related to the fact that the western Pacific in its background state is more La Niña-like and that El Niños intrude as distinct events (Kessler 2002) and the asymmetric warm water volume discharge/recharge between El Niño and La Niña events (Meinen and McPhaden 2000). Therefore, extended, albeit weak, La Niña anomalies persisting for up to two years, allow the gradual build-up and transmission of the Pacific signal to the eastern Indian Ocean earlier in the year, than is the case for the more seasonally phase-locked El Niño and low eIO heat content events. The point of origin of the positive/negative anomalies during high/low heat content events also differs between the two cases: in the low events, negative anomalies first appear in the coastal upwelling region off Java and Sumatra in July; on the other hand, high heat content events first feature Indian Ocean heat content anomalies on the northwest shelf region off Australia, from where anomalies spread to the northwest and southwards over time. The role of the heat content anomalies in the western Pacific for eastern Indian Ocean heat content thus seems to differ between the two cases: while western Pacific heat content anomalies appear to be instrumental during the formation of high heat content events, they are just symptomatic of the large-scale circulation during low heat content events. This will be explored in more detail in the following Section for several key regions around the Indonesian archipelago.

b. Evolution of heat content anomalies in three key regions

To assess the model representation of upper-ocean variability in more detail in three key locations around the Indonesian archipelago, the seasonal cycle and anomaly time-series of observed and model SSH are shown in Fig. 10 for the regions indicated by the boxes in Fig. 3h. Observed SSH is based on remotely sensed data from Aviso for the period 1993–2004, while the modeled SSH is for 1970–2004 from the control simulations at 0.5° and 0.25° horizontal resolution, respectively. The three regions are as follows: the eastern Indian Ocean region, "eIO"; the northwest shelf off Australia, "NWAus", 105°–115°E and 10°–20°S, and the Celebes Sea, 125°–130°E and 2°–6°N.

The seasonal cycle of observed SSH in the eIO region is moderately negative during the first few months of the year (Fig. 10a). SSH peaks during May and June with values in excess of 5cm, before rapidly declining with the onset of the southeasterly monsoon and the associated coastal upwelling off Sumatra, reaching a minimum in September, before moderately positive values at the end of the year. This semiannual signal is due to the Yoshida-Wyrtki jet (Yoshida 1959; Wyrtki 1973) excited during the two monsoon breaks. Overall, the modeled SSH capture the seasonal cycle in SSH very well for the eIO region. The anomaly time-series for eIO SSH also indicate good agreement for the overlapping analysis period 1993–2004 between model and observed (Fig. 10e). The overall close match in the eIO SSH seasonal cycle and anomaly time-series (Fig. 10a,e) between the two control simulations with differing horizontal resolution suggests that the results presented here are not model resolution dependent.

For the NWAus region, the observed seasonal cycle in SSH is characterized by a minimum in February and March, a fairly broad maximum during austral winter (May–August), and lower values from October onwards (Fig. 10b). In the model simulations, the general shape of the NWAus SSH seasonal cycle is captured, but shifted forward by a month compared to the observed. It has to be noted that the SSH seasonal cycle in the model is based on the longer period 1970–2004, compared to 1993–2004 for the observed. When comparing SSH for the shorter, common period 1993–2004 between the model and observed (figure not shown), the seasonal cycles are more closely aligned. This suggests that decadal and long-term trends in SSH and upper-ocean variability exist for the NWAus region. Further exploration of decadal variability in Indian Ocean heat content (cf. Feng et al. 2011; Schwarzkopf and Böning 2011) and longer-term changes are beyond the scope of the present study and will be addressed elsewhere.

The amplitude of the seasonal cycle of SSH is comparable between the eIO and NWAus region (Fig. 10a,b). In contrast, interannual variations of SSH for NWAus generally exhibit more frequent, larger anomalies than seen for the eIO region (Fig. 10d,e). In particular, frequent positive SSH anomalies of considerable magnitude are apparent for NWAus, while eIO SSH anomalies seem to be characterized by larger negative excursions, such as in 1994 and 1997. These results are consistent with our earlier findings: i.e. that low eIO heat content events are of larger magnitude than positive events (cf. Fig. 5); and that the NWAus region exhibits strong signals during positive heat content events, but not during low events (cf. Fig. 9). As such, Fig. 10 further supports the notion that asymmetric behavior across the eastern Indian Ocean is not restricted to the eIO region.

For the Celebes Sea in the western Pacific, the observed SSH seasonal cycle is characterized by a minimum during austral summer, while positive anomalies dominate between April–October (Fig. 10c). Interannual variations in SSH in the Celebes Sea are largest of the three regions, varying between ± 0.15m (Fig. 10f), consistent with large excursions of the thermocline in the western Pacific warm pool area (e.g., Williams and Grottoli 2010). Observed and modeled interannual anomalies of SSH in the Celebes Sea, as in the other two regions, are in close agreement.

For the three key regions, it is of interest to assess how the seasonal cycle of heat content during low and high events deviates from the long-term seasonal cycle based on all years. Fig. 11 shows the seasonal cycle of heat content for the three regions for the CTRL, PO_{HF+WS}, and IO_{HF+WS} simulations. The thick black line reproduces the long-term seasonal cycle of all 35 years in the CTRL. For the seven low/high heat content events, the composite seasonal cycle for the specific experiment is indicated with blue/red lines, along with the values in individual years in the two cases with blue/red dots, respectively. To determine whether the composite cycle during low/high events in the specific experiments deviates significantly from the long-term seasonal cycle expected for all years in the CTRL, a Monte Carlo approach was used (cf. Ummenhofer et al. 2011): From all 35 years in the CTRL simulation, seven years were randomly selected and their mean seasonal cycle determined. This was repeated 25,000 times, resulting in a probability density function of expected heat content for a set of seven years, against which the composite heat content during the seven low/high events could be compared in the different experiments. Gray shading in Fig. 11 shows the lower and upper bounds of a 90% confidence interval for the randomly generated distribution based on all years. Where the blue/red line lies outside the gray shading, the values differ significantly from the long-term seasonal cycle in the CTRL.

In the CTRL, it is apparent that eIO heat content during low/high events deviates significantly from the long-term seasonal cycle from August onwards (Fig. 11a). The seasonal reduction in heat content during July–September is amplified and prolonged during low heat content events, while the seasonal decline is damped in the high events. During the first half of the year, the eIO seasonal cycle during low/high events is largely indistinguishable from average years, with the exception of slightly enhanced heat content during January and February in high heat content events. In contrast, NWAus heat content in the CTRL is characterized by significantly higher values throughout the year during high heat content events (Fig. 11b). A significant reduction in the NWAus heat content during low events does not occur until August. In the Celebes Sea, significantly enhanced heat content is apparent throughout the year for high events, while the onset of significant reductions in the low heat content events is delayed until April. These findings are consistent with earlier results (cf. Figs. 9) and support the notion that it is the delayed build-up of western Pacific heat content anomalies that contributes towards the differential behavior of upper-ocean thermal properties over the NWAus region and the broader eastern Indian Ocean.

The PO_{HF+WS} and IO_{HF+WS} experiments (Fig. 11d,g) further highlight that low eIO heat content events require atmospheric forcing over the Indian Ocean region to reproduce the anomalous reduction in heat content in the second half of the year seen in the CTRL: only in IO_{HF+WS} are July–December heat content anomalies of comparable magnitude to the CTRL produced; in the PO_{HF+WS} experiment low events are characterized by marginally significant, but consistently below-average eIO heat content from January to September, but lack the characteristic amplification of the seasonal cycle during austral spring. High heat content events in the eIO only show some significantly enhanced anomalies post-September in the IO_{HF+WS} case, most likely related to the tropical heat content signal forced by local winds (cf. Fig. 8). For the eIO region, high heat content events do not otherwise exhibit significant deviations prior to September for IO_{HF+WS} or at any time during the year for PO_{HF+WS}. Over the NWAus region, high heat content events in the PO_{HF+WS} simulation show significantly enhanced heat content throughout the year, while they are only very slightly above-average in the IO_{HF+WS} case (Fig. 11e,h). Neither of the two experiments records significant deviations during low events, which is in contrast to the CTRL. The exact reason for this is unclear, but implies some non-linear interaction between the two ocean basins in the case of the CTRL. The gap in the wind forcing over the Indonesian archipelago that is not represented in either the IO_{HF+WS} or the PO_{HF+WS} case can also not be discounted. In the Celebes Sea, anomalous high heat content already builds up by the start of the year in PO_{HF+WS}, while a significant reduction for low events is not apparent until several months later (Fig. 11f).

7. Implications for predictability

The difference in timing and evolution of subsurface heat content in the western Pacific between low and high heat content events (cf. Figs. 9,11) indicates that the role of western Pacific anomalies for eastern Indian Ocean variability is distinct between the two events: during low eIO events, western Pacific heat content anomalies develop simultaneously with eastern Indian anomalies and thus are symptomatic of the large-scale circulation; however, the gradual build-up of western Pacific anomalies, probably related to the longer lasting, albeit weaker, high heat content anomalies associated with La Niña states (Kessler 2002), seems instrumental for the formation of high events in the eastern Indian Ocean. The latter case, with its extended evolution, has implications for predicting eastern Indian Ocean upper-ocean heat content.

To explore the potential utility for predictions further, we used Celebes Sea subsurface heat content as a predictor for upper-ocean properties across the eastern Indian Ocean during

SON. Using the methodology described previously for eIO heat content events, years were determined in the CTRL that showed anomalous high heat content anomalies in the Celebes Sea region during March–May (MAM) and JJA. Composites of SST, SSH, and heat content during SON are shown across the Indo-Pacific for high heat content events during MAM and JJA in the Celebes Sea at 6-month and 3-month lead, respectively (Fig. 12).

The SON anomalies during years that had shown anomalously high heat content in the Celebes Sea six months previously are characterized by warm SST in the eastern Indian Ocean, around the Indonesian archipelago, and over much of the southwestern Pacific (170°E–160°W, 20°–40°S; Fig. 12a). Positive SSH and heat content anomalies occur across the eastern Indian Ocean, including the Leeuwin Current region, the northwest shelf off Australia, the Indonesian archipelago, and the western equatorial Pacific (Fig. 12c,e). In the central subtropical Indian Ocean (50°–90°E, 10°–20°S) negative SSH and heat content anomalies are apparent. Years with anomalously high JJA Celebes Sea heat content show very similar SON anomaly patterns across the eastern Indian Ocean to those at 6-month lead. The magnitude of western Pacific anomalies is intensified at 3-month lead, and the spatial extent of the anomalies more closely restricted to the eastern Indian Ocean region and the Indonesian archipelago, compared to the 6-month lead.

8. Summary and conclusions

We have investigated the well-known asymmetry in the magnitude of anomalies in eIO variability (e.g., Hong and Li 2010; Zheng et al. 2010) using ocean model hindcast simulations. Sensitivity experiments with variable wind field forcing in the Indian and Pacific

Oceans were used to distinguish the role of air-sea feedbacks in the Indian Ocean region and remote forcing from the Pacific for low and high heat content events across the eastern Indian Ocean. Composites during SON of low and high eIO heat content events revealed marked differences in the broad features of the anomalies across the eastern Indian Ocean between the two cases, not limited to the eIO region that previous studies have focused on (e.g., Hong et al. 2008a,b; Zheng et al. 2010). Low heat content events were characterized by a zonal gradient in SST, SSH, and heat content anomalies across the tropical Indian Ocean, with anomalous shoaling in the east and deepening of the thermocline in the west. In contrast, high heat content events, while also exhibiting a zonal component, were dominated by a meridional gradient in SST, SSH, and heat content across the eastern Indian Ocean, with tropical and subtropical anomalies indicative of a deepening and shoaling thermocline, respectively.

In addition to the spatial differences, the temporal evolution of the eastern Indian Ocean heat content anomalies was distinct between the low and high heat content events: anomalies in the low events developed rapidly in the second half of the year from July onwards; in contrast during high events, the evolution of positive anomalies was much slower, but progressed from the start of the year already. This could be related to differences in the build-up of heat content anomalies in the western Pacific Ocean, which differed markedly between the two cases, implying a different role for the remote Pacific contributions: while western Pacific heat content anomalies appeared to be instrumental during the formation of high eIO heat content events, they seemed just symptomatic of the large-scale circulation during low heat content events. This is most likely related to the asymmetric warm water volume discharge/recharge during ENSO events in the western Pacific (Meinen and

McPhaden 2000) and the extended presence of La Niña-like high heat content anomalies (Kessler 2002). The latter enables an earlier transmission of the signal to the eastern Indian Ocean in the year and thus a larger remote contribution to high eIO heat content events than during low ones.

Given the role of the Pacific for high heat contents in the eastern Indian Ocean, decadal variations in the thermocline of the western tropical Pacific are of interest: corals off the island of Palau, at 7°N and 134°E within the region of high heat content in the western Pacific during high eIO events, record a shoaling in the thermocline over recent decades, which has been linked to the shift in the Pacific Decadal Oscillation (Williams and Grottoli 2010). Over the period 1977–1998, the western tropical Pacific thermocline shoaled considerably, from much deeper thermocline levels in the late 1960s and early 1970s, the latter characterized by a spate of eIO high heat content events (1970, 1971, 1973, 1974, 1975; Fig. 5). To ascertain any such link further, more research is required into the role of western Pacific forcing for low/high eastern Indian Ocean heat content events on decadal timescales (cf. Schwarzkopf and Böning 2011), which is beyond the scope of the present study.

The results here indicate that subsurface heat content in the Celebes Sea could be useful for predicting high heat content events across the eastern Indian Ocean. Subsurface heat content reflects upper-ocean thermal properties and changes in the thermocline, and is linked closely to SSH, in itself a proxy for variations in thermocline depth (Hong and Li 2010). Remotely sensed SSH for the western Pacific could therefore be useful for predictive purposes of eastern Indian Ocean upper-ocean thermal properties during high heat content events. The surface manifestation of these high heat content events in eastern Indian Ocean anomalies are reminiscent of patterns previously shown to affect regional rainfall for Australia (Ummenhofer et al. 2008, 2009b). Thus, we have described how atmospheric remote forcing from the Pacific contributes to Indian Ocean conditions that affect regional climate via an oceanic teleconnection between the western Pacific and eastern Indian Ocean over extended timescales. The mechanism for the transmission of Pacific wind forcing is based on coastal wave dynamics (cf. Clarke and Liu 1994; Wijffels and Meyers 2004, and references therein) and has previously been linked to the transmission of ENSO to Western Australian sea level variations and Leeuwin Current strength (Cai et al. 2005; Shi et al. 2007; Feng et al. 2011). Here we have expanded on this previous work to elucidate the role of remote contributions from the Pacific to understand broader asymmetries across the eastern Indian Ocean as seen during opposite phases of IOD events, beyond the eIO region and local air-sea feedbacks detailed in earlier work. The Indian Ocean can thus act as a mediator for transmitting remote Pacific forcing to the Australian region, as previously shown by Taschetto et al. (2011) during ENSO events. This "slow" teleconnection could be exploited for improved long-range forecasts of benefit to a dry continent characterized by a highly variable climate.

Acknowledgments.

We are grateful for the following observational products: HadISST from the UK Met Office and SSH anomalies from Ssalto/Duacs provided by the Aviso CNES Data Center. The integration of the experiments has been performed at the North-German Supercomputing Alliance (HLRN) and the Computing Centre at Kiel University. CCU gratefully acknowledges financial support by the research cluster of excellence "The Future Ocean", IFM-GEOMAR, Kiel, Germany, and the Australia-Germany Researcher Mobility Call by the Australian Academy of Science. FUS was supported by the DFG through SFB754 (www.sfb754.de). Helpful discussions with J. McCreary, University of Hawaii, USA, are gratefully acknowledged. An earlier version of the manuscript benefitted from comments by three anonymous reviewers.

REFERENCES

Alory, G., S. Wijffels, and G. Meyers, 2007: Observed temperature trends in the Indian Ocean over 1960–1999 and associated mechanisms. *Geophysical Research Letters*, **34 (L02606)**, doi:10.1029/2006GL028 044.

Annamalai, H., J. Potemra, R. Murtugudde, and J. P. McCreary, 2005: Effect of preconditioning on the extreme climate events in the tropical Indian Ocean. *Journal of Climate*, **18**, 3450–3469.

Cai, W., G. Meyers, and G. Shi, 2005: Transmission of ENSO signal to the Indian Ocean. *Geophysical Research Letters*, **32 (L05616)**, doi:10.1029/2004GL021 736.

Cai, W., A. Sullivan, and T. Cowan, 2008: Shoaling of the off-equatorial south indian ocean thermocline: Is it driven by anthropogenic forcing? *Geophysical Research Letters*, **35 (L12711)**, doi:10.1029/2008GL034 174.

Clarke, A. J. and X. Liu, 1994: Interannual sea level in the northern and eastern Indian Ocean. *Journal of Physical Oceanography*, **24**, 1224–1235.

Collins, M., et al., 2010: The impact of global warming on the tropical Pacific and El Niño. *Nature Geoscience*, **3**, 391–397.

Feng, M., A. Biastoch, C. Böning, N. Caputi, and G. Meyers, 2008: Seasonal and interannual variations of upper ocean heat balance off the west coast of Australia. *Journal of Geophysical Research*, **113 (C12025)**, doi:10.1029/2008JC004 908.

Feng, M., C. Böning, A. Biastoch, E. Behrens, E. Weller, and Y. Masumoto, 2011: The reversal of the multi-decadal trends of the equatorial Pacific easterly winds, and the Indonesian Throughflow and Leeuwin Current transports. *Geophysical Research Letters*, **38 (L11604)**, doi:10.1029/2011GL047 291.

Fischer, A. S., P. Terray, E. Guilyardi, S. Gualdi, and P. Delecluse, 2005: Two independent triggers for the Indian Ocean Dipole/Zonal Mode in a coupled GCM. *Journal of Climate*, **18**, 3428–3449.

Griffies, S. M., et al., 2009: Coordinated Ocean-ice Reference Experiments (COREs). *Ocean Modelling*, **26**, 1–46.

Hendon, H. H. and G. Wang, 2010: Seasonal prediction of the Leeuwin Current using the POAMA dynamical seasonal forecest model. *Climate Dynamics*, **34**, 1129–1137.

Hendon, H. H., 2003: Indonesian rainfall variability: Impacts of ENSO and local air-sea interaction. *Journal of Climate*, **16**, 1775–1790.

Hong, C.-C., T. Li, LinHo, and J.-S. Kug, 2008a: Asymmetry of the Indian Ocean Dipole. Part I: Observational analysis. *Journal of Climate*, **21**, 4834–4848.

Hong, C.-C., T. Li, and J.-J. Luo, 2008b: Asymmetry of the Indian Ocean Dipole. Part II: Model diagnosis. *Journal of Climate*, **21**, 4849–4858.

Hong, C.-C. and T. Li, 2010: Independence of SST skewness from thermocline feedback in the eastern equatorial Indian Ocean. *Geophysical Research Letters*, **37 (L11702)**, doi:10.1029/2010GL043 380.

Kessler, W. S., 2002: Is ENSO a cycle or a series of events? *Geophysical Research Letters*, **29 (23)**, doi:10.1029/2002GL015 924.

Large, W. and S. Yeager, 2004: Diurnal to decadal global forcing for ocean and seaice models: the data sets and climatologies. Tech. rep., TN-460+STR, National Center for Atmospheric Research, Boulder, USA, pp. 105, 105 pp.

Li, T., B. Wang, C.-P. Chang, and Y. Zhang, 2003: A theory for the Indian Ocean dipole-zonal mode. *Journal of the Atmospheric Sciences*, **60**, 2119–2135.

Li, T., Y. Zhang, E. Lu, and D. Wang, 2002: Relative role of dynamic and thermodynamic processes in the development of the Indian Ocean Dipole: An OGCM diagnosis. *Geophysical Research Letters*, **29 (23)**, doi:10.1029/2002GLGL015 789.

Madec, G., 2007: NEMO ocean engine, version 3.1. Tech. rep., Note Pôle Model. Inst. Pierre-Simon Laplace, Paris, 27, 27 pp.

Meinen, C. S. and M. J. McPhaden, 2000: Observations of warm water volume changes in the equatorial Pacific and their relationship to El Niño and La Niña. *Journal of Climate*, **13**, 3551–3559.

Meyers, G., P. McIntosh, L. Pigot, and M. Pook, 2007: The years of El Niño, La Niña and interactions with the tropical Indian Ocean. *Journal of Climate*, **20**, 2872–2880.

Meyers, G., 1996: Variation of Indonesian throughflow and the El-Niño-Southern Oscillation. *Journal of Geophysical Research*, **101**, 12 255–12 263.

Rao, S. A., S. K. Behera, Y. Masumoto, and T. Yamagata, 2002: Interannual subsurface variability in the tropical Indian Ocean with a special emphasis on the Indian Ocean Dipole. *Deep-Sea Research II*, **49 (7-8)**, 1549–1572.

Rayner, N. A., D. E. Parker, E. B. Horton, C. K. Folland, L. V. Alexander, and D. P. Rowell, 2003: Global analyses of SST, sea ice and night marine air temperature since the late nineteenth century. *Journal of Geophysical Research*, **108 (4407)**, doi:10.1029/2002JD002 670.

Saji, N. H., B. N. Goswami, P. N. Vinayachandran, and T. Yamagata, 1999: A dipole mode in the tropical Indian Ocean. *Nature*, **401**, 360–363.

Santoso, A., A. Sen Gupta, and M. H. England, 2010: Genesis of Indian Ocean mixed layer temperature anomalies: A heat budget analysis. *Journal of Climate*, **23**, 5375–5403.

Schott, F. A., S.-P. Xie, and J. McCreary, J. P., 2009: Indian Ocean variability and climate variability. *Reviews of Geophysics*, **47 (RG1002)**, doi:10.1029/2007RG000 245.

Schwarzkopf, F. U. and C. W. Böning, 2011: Contribution of Pacific wind stress to multidecadal variations in upper-ocean heat content and sea level in the tropical south Indian Ocean. *Geophysical Research Letters*, **38 (L12602)**, doi:10.1029/2011GL047 651.

Shi, G., J. Ribbe, W. Cai, and T. Cowan, 2007: Multidecadal variability in the transmission of ENSO signals to the Indian Ocean. *Geophysical Research Letters*, **34 (L09706)**, doi:10.1029/2007GL029 528.

Sinha, A., L. Stott, M. Berkelhammer, H. Cheng, R. L. Edwards, B. Buckley, M. Aldenderfer, and M. Mudelsee, 2011: A global context for megadroughts in monsoon Asia during the past millennium. *Quaternary Science Reviews*, **30**, 47–62.

Taschetto, A. S., A. Sen Gupta, H. H. Hendon, C. C. Ummenhofer, and M. H. England, 2011: The relative contribution of Indian Ocean sea surface temperature anomalies on Australian summer rainfall during El Niño events. *Journal of Climate*, **24**, 3734–3747.

Ummenhofer, C. C., M. H. England, P. C. McIntosh, G. A. Meyers, M. J. Pook, J. S. Risbey, A. Sen Gupta, and A. S. Taschetto, 2009a: What causes Southeast Australia's worst droughts? *Geophysical Research Letters*, **36 (L04706)**, doi:10.1029/2008GL036 801.

Ummenhofer, C. C., A. Sen Gupta, M. J. Pook, and M. H. England, 2008: Anomalous rainfall over southwest Western Australia forced by Indian Ocean sea surface temperatures. *Journal of Climate*, **21**, 5113–5134.

Ummenhofer, C. C., A. Sen Gupta, A. S. Taschetto, and M. H. England, 2009b: Modulation of Australian precipitation by meridional gradients in East Indian Ocean sea surface temperature. *Journal of Climate*, **22**, 5597–5610.

Ummenhofer, C. C., et al., 2011: Indian and Pacific Ocean influences on Southeast Australian drought and soil moisture. *Journal of Climate*, **24**, 1313–1336.

Webster, P. J., A. M. Moore, J. P. Loschnigg, and R. R. Leben, 1999: Coupled ocean-atmosphere dynamics in the Indian Ocean during 1997–98. *Nature*, **401**, 356–360.

Wijffels, S. and G. Meyers, 2004: An intersection of oceanic waveguides - variability in the Indonesian Throughflow region. *Journal of Physical Oceanography*, **34**, 1232–1253.

Williams, B. and A. G. Grottoli, 2010: Recent shoaling of the nutricline and thermocline in the western tropical Pacific. *Geophysical Research Letters*, **37 (L22601)**, doi:10.1029/2010GL044 867.

Wu, R., B. P. Kirtman, and V. Krishnamurthy, 2008: An asymmetric mode of tropical Indian Ocean rainfall variability in boreal spring. *Journal of Geophysical Research*, **113 (D05104)**, doi:10.1029/2007JD009 316.

Wyrtki, K., 1973: An equatorial jet in the Indian Ocean. *Science*, **181**, 262–264.

Yoshida, K., 1959: A theory of the Cromwell current and of the equatorial upwelling - An interpretation in a similarity to a coastal circulation. *Journal of the Oceanographical Society of Japan*, **15**, 159–170.

Zheng, X.-T., S.-P. Xie, G. A. Vecchi, Q. Liu, and J. Hafner, 2010: Indian Ocean Dipole response to global warming: Analysis of ocean-atmospheric feedbacks in a coupled model. *Journal of Climate*, **23**, 1240–1253.

List of Figures

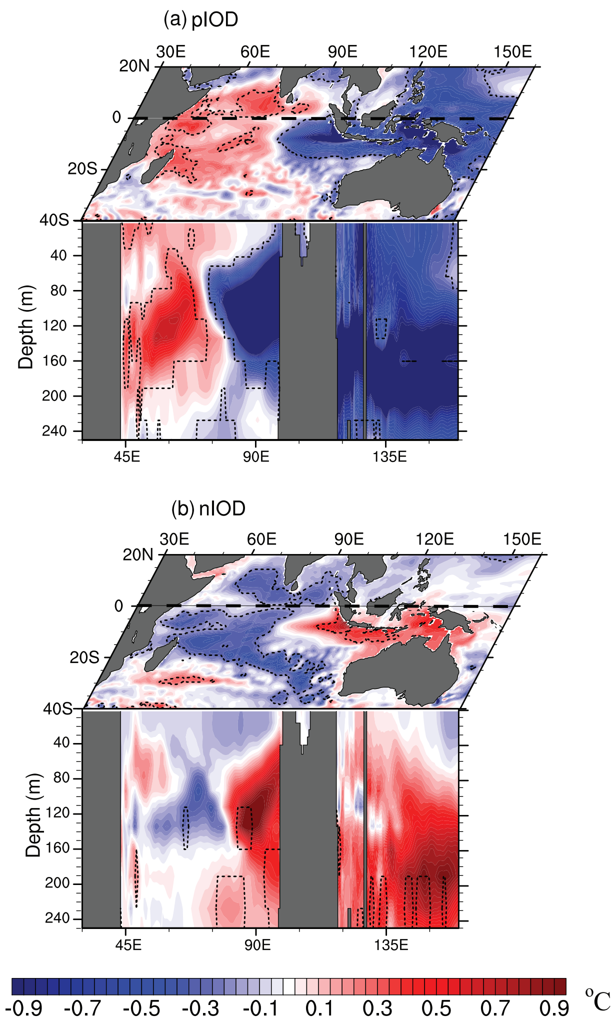

FIG. 1. Schematic of (a) positive and (b) negative IOD events: composite temperature anomalies for the surface and an equatorial cross-section during September–November for the period 1970–2004 from the control simulations. Positive/negative IOD years were based on the classification by Meyers et al. (2007) and updated by Ummenhofer et al. (2009a). The area enclosed by the dashed contours denotes anomalies that are significant at the 80% level as estimated by a two-tailed t-test.

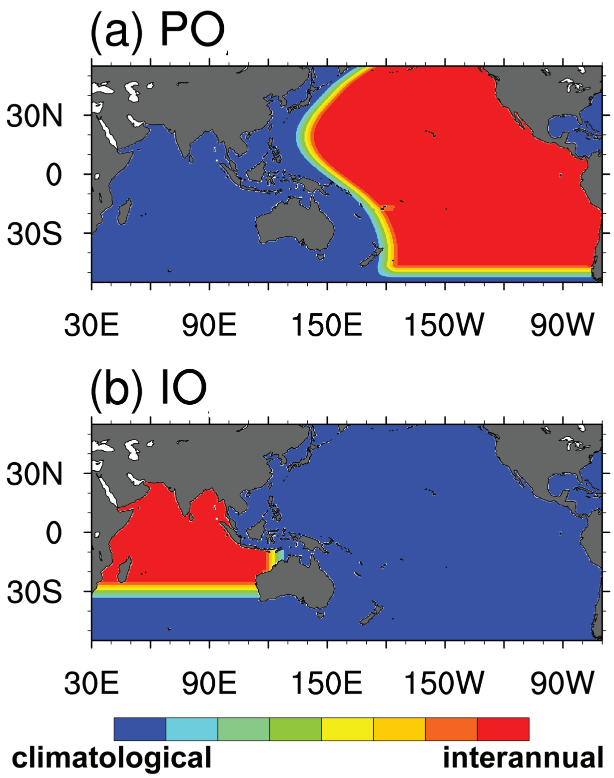

FIG. 2. Masks used in the model perturbation experiments: masks in (a) Pacific and (b) Indian Ocean experiments to highlight areas of climatological and interannual forcing for the Indo-Pacific region. For further details refer to Table 1.

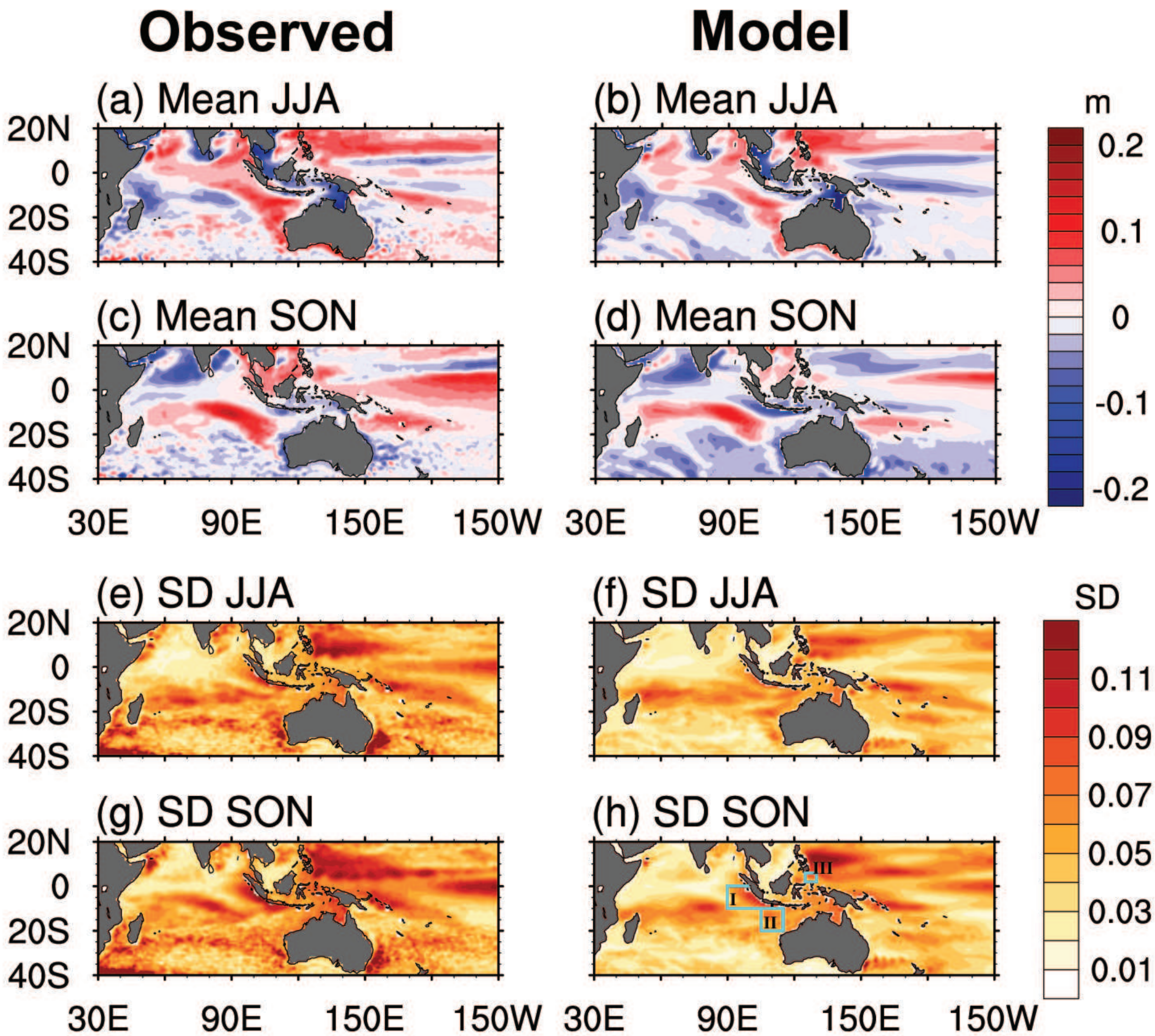

FIG. 3. Comparison of model and observed SSH in the Indo-Pacific: (a–d) seasonal deviation from the long-term mean and (e–h) seasonal standard deviation for (left) observed and (right) control simulation for the period 1993–2004. The blue boxes in (h) indicate regions used for further time-series analysis, namely I “eIO”, II “NWAus”, and III “Celebes”.

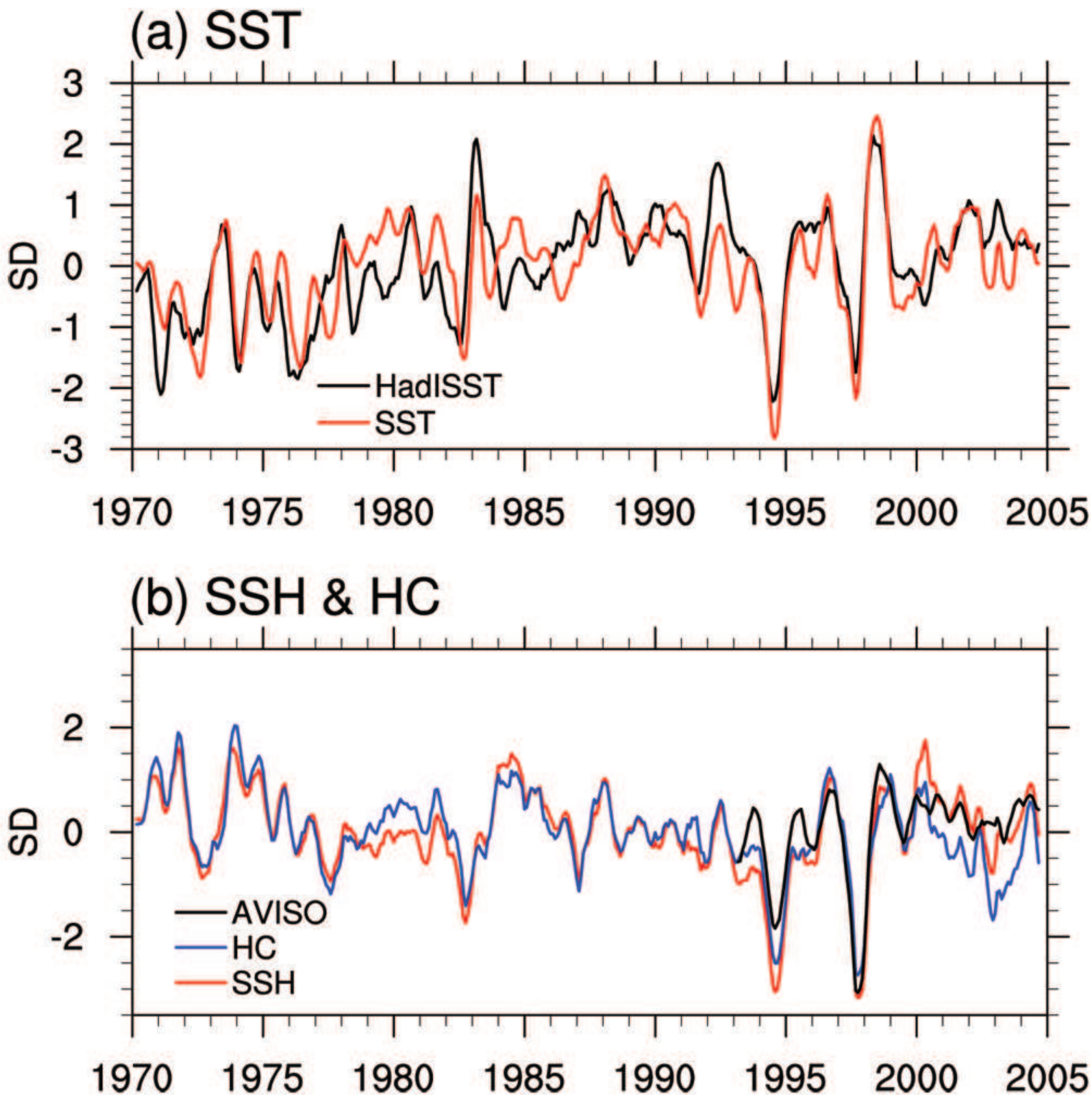

Fig. 4. Comparison of model and observed time-series in the eIO region: normalized 6-month running mean of (a) SST (°C) and (b) SSH (cm) and heat content (°C m) area-averaged over box I in Fig. 3. The analysis periods shown are 1970–2004 for model and HadISST, while Aviso SSH is only for 1993–2004.

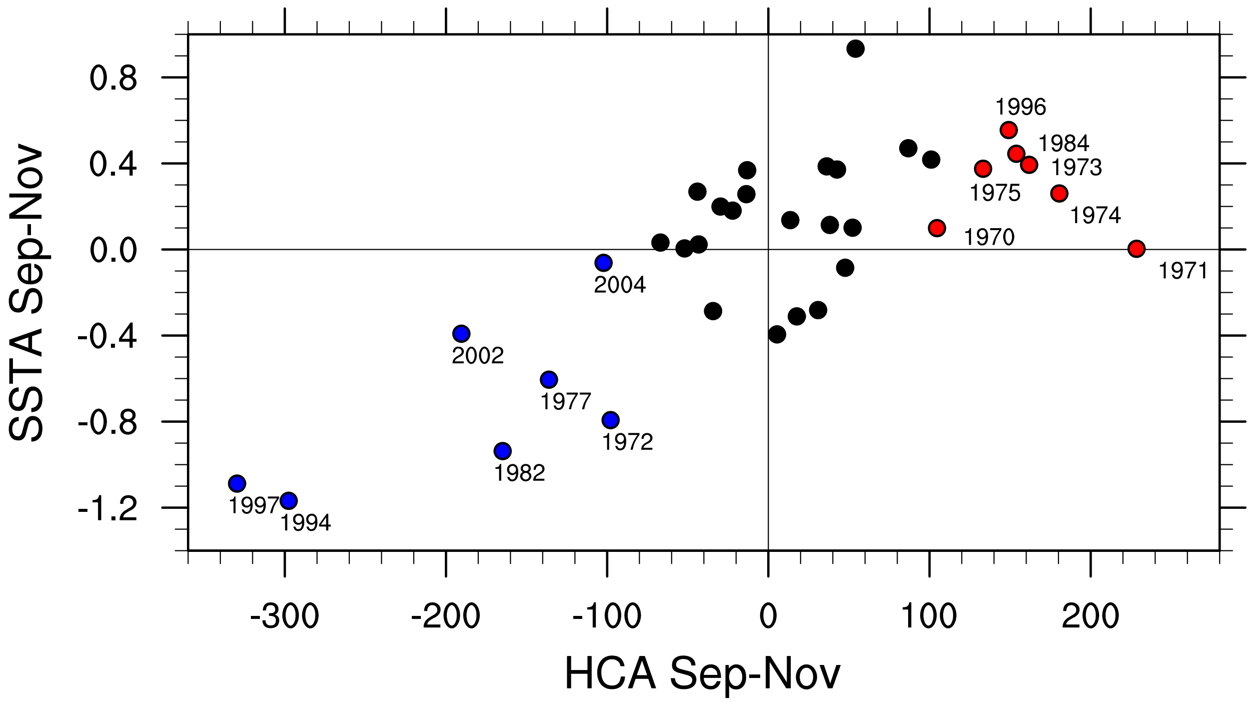

FIG. 5. Asymmetry in eIO SST and heat content anomalies: SST anomalies (°C) versus heat content anomalies (°C m) averaged for September–November in the control simulation for the period 1970–2004. The years with anomalous high (low) heat content have been highlighted with red (blue) circles, respectively.

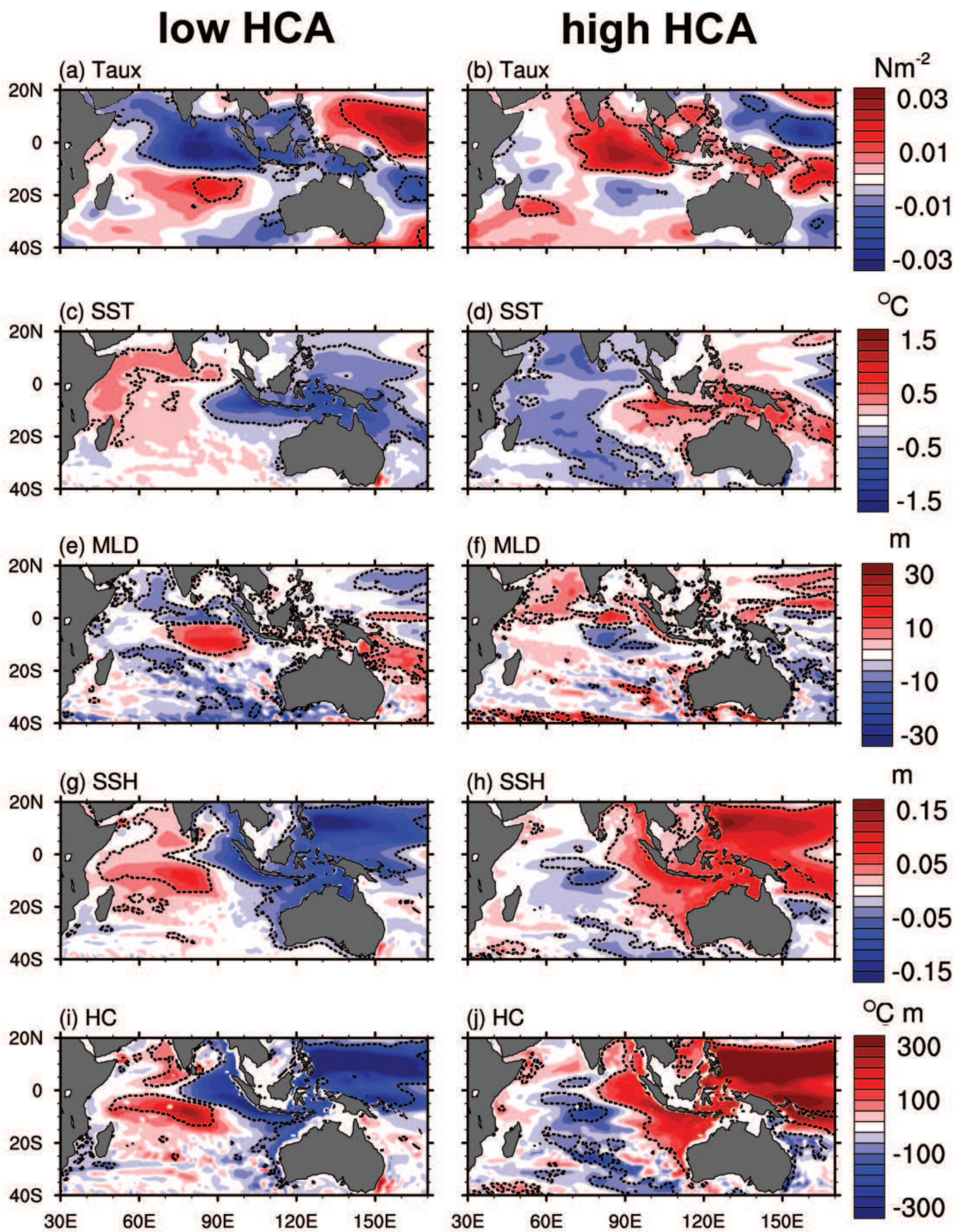
low HCA
high HCA
(a) Taux
(b) Taux
Nm-2
0.03
0.01
-0.01
-0.03
(c) SST
(d) SST
°C
1.5
0.5
-0.5
-1.5
(e) MLD
(f) MLD
m
30
10
-10
-30
(g) SSH
(h) SSH
m
0.15
0.05
-0.05
-0.15
(i) HC
(j) HC
°C m
300
100
-100
-300
20N
0
20S
40S
30E
60E
90E
120E
150E

FIG. 6. Composite anomalies in the control simulation for the period 1970–2004 for anomalous low (left), anomalous high (right) eIO heat content events. Anomalies are shown for (a–b) zonal wind stress (N m^{-2}), (c–d) SST (°C), (e–f) mixed layer depth (m), (g–h) SSH (m), and (i–j) heat content (°C m). The area enclosed by the dashed contours denotes anomalies that are significant at the 90% level as estimated by a two-tailed t-test.

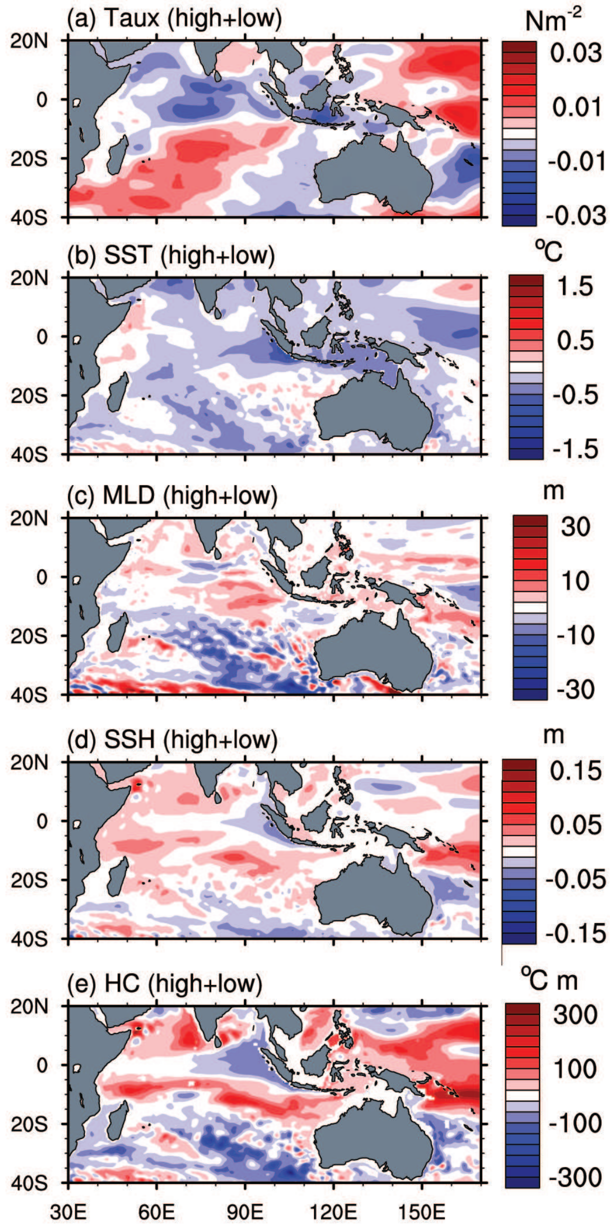

FIG. 7. Sum of the composite anomalies in the control simulation for the period 1970–2004 by adding the anomalies for low (left) and high (right) eIO heat content events in Fig. 6. The sum of anomalies is shown for (a) zonal wind stress (N m^{-2}), (b) SST (°C), (c) mixed layer depth (m), (d) SSH (m), and (e) heat content (°C m).

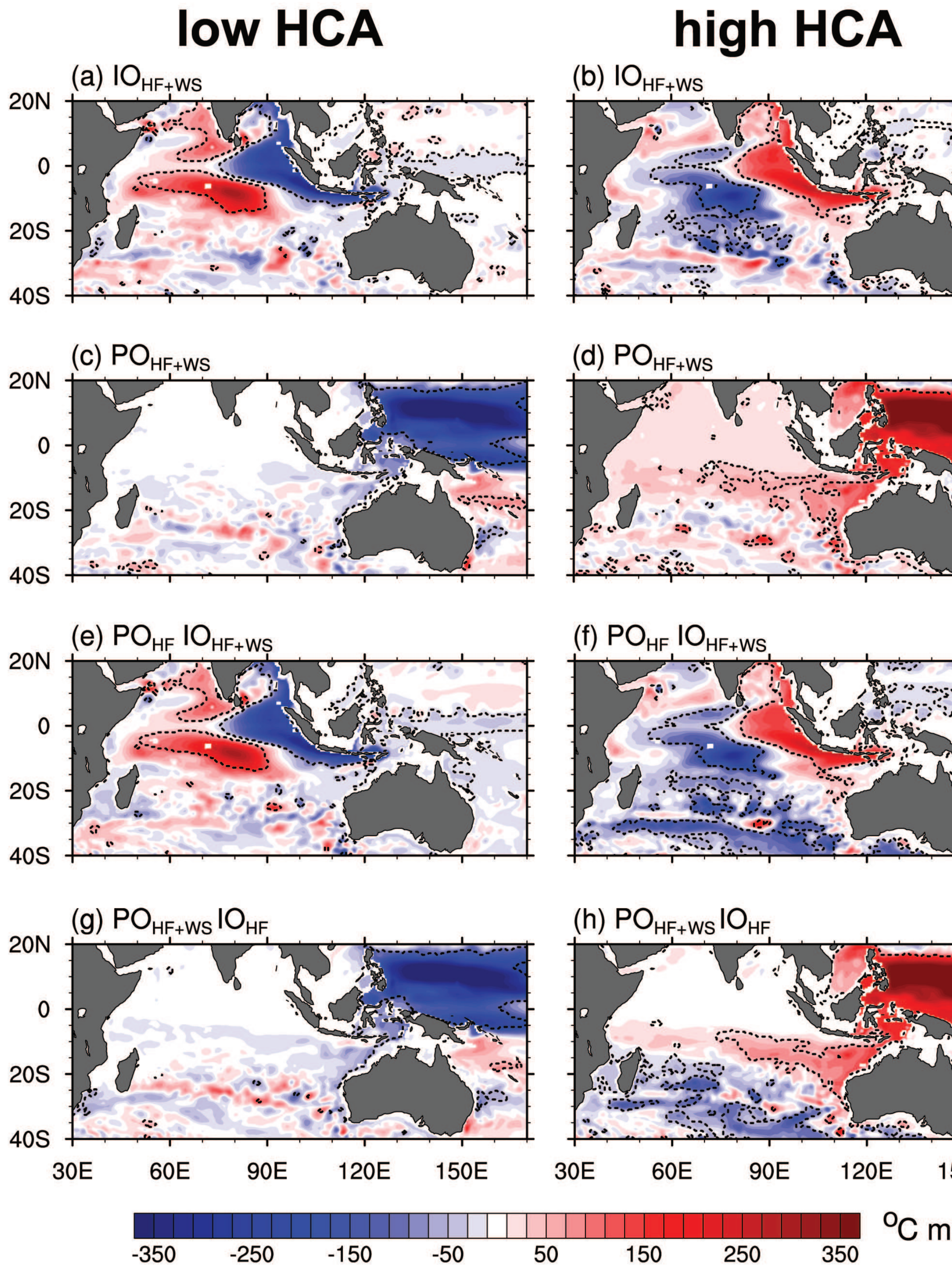
low HCA
high HCA
(a) IO$_{HF+WS}$
(b) IO$_{HF+WS}$
(c) PO$_{HF+WS}$
(d) PO$_{HF+WS}$
(e) PO$_{HF}$ IO$_{HF+WS}$
(f) PO$_{HF}$ IO$_{HF+WS}$
(g) PO$_{HF+WS}$ IO$_{HF}$
(h) PO$_{HF+WS}$ IO$_{HF}$
20N
0
20S
40S
30E
60E
90E
120E
150E
-350
-250
-150
-50
50
150
250
350
^{o}C m

Fig. 8. Role of remote and local forcing for Indian Ocean heat content: Composite anomalies of heat content (°C m) during anomalous low (left) and high (right) eIO heat content events, as defined in the control simulation, in the following experiments for September–November for the period 1970–2004: (a–b) IO_{HF+WS}, (c–d) PO_{HF+WS}, (e–f) PO_{HF} IO_{HF+WS}, and (g–h) IO_{HF} PO_{HF+WS}. The area enclosed by the dashed contours denotes anomalies that are significant at the 90% level as estimated by a two-tailed t-test.

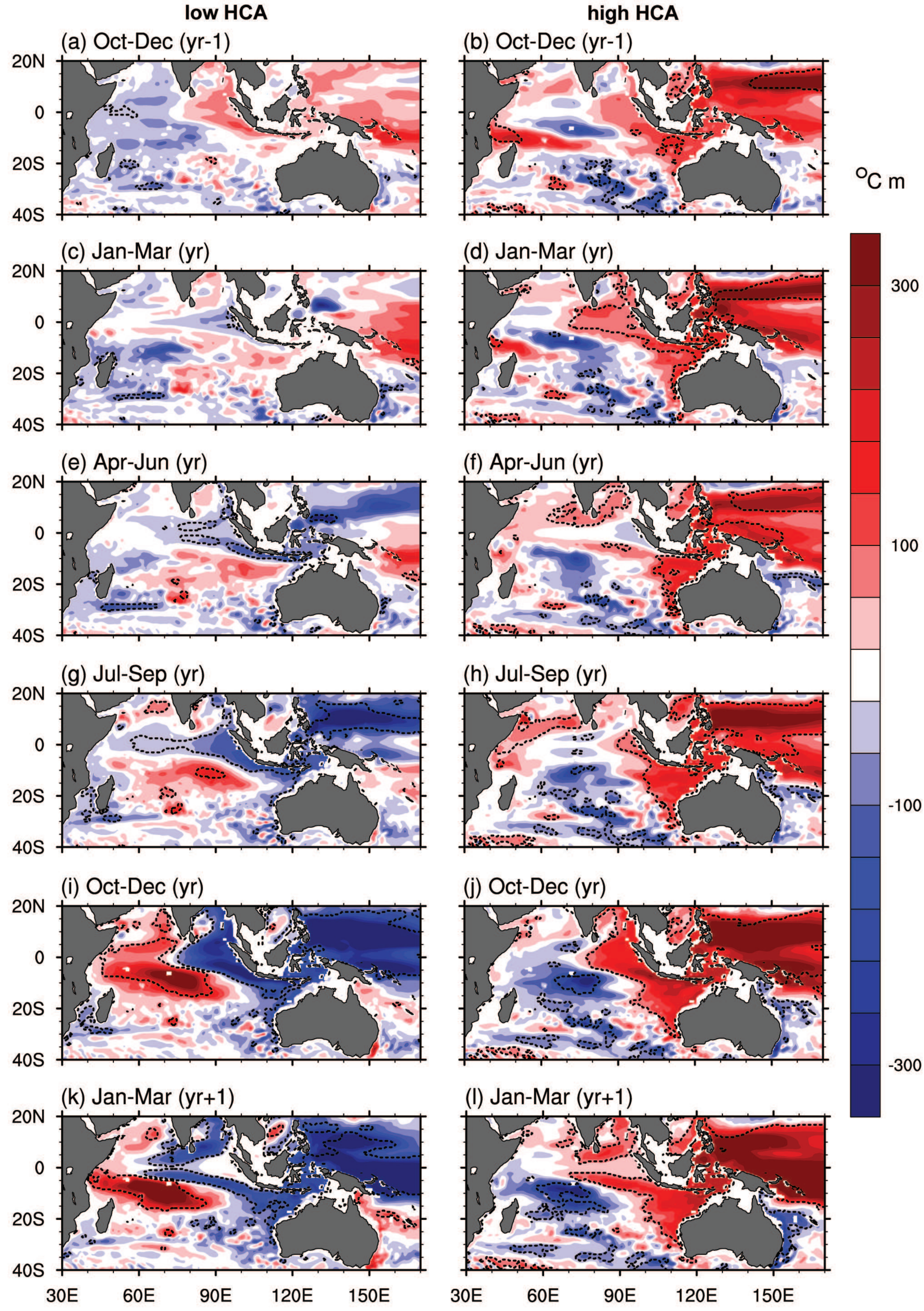

low HCA
high HCA
(a) Oct-Dec (yr-1)
(b) Oct-Dec (yr-1)
(c) Jan-Mar (yr)
(d) Jan-Mar (yr)
(e) Apr-Jun (yr)
(f) Apr-Jun (yr)
(g) Jul-Sep (yr)
(h) Jul-Sep (yr)
(i) Oct-Dec (yr)
(j) Oct-Dec (yr)
(k) Jan-Mar (yr+1)
(l) Jan-Mar (yr+1)
20N
0
20S
40S
30E
60E
90E
120E
150E
°C m
300
100
-100
-300

FIG. 9. Evolution of Indian Ocean heat content anomalies in the control simulations: composite anomalies of seasonal heat content (°C m) leading into (yr-1) and out of (yr+1) low (left) and high (right) heat content events (yr), as defined in the control simulation for the period 1970–2004. The area enclosed by the dashed contours denotes anomalies that are significant at the 90% level as estimated by a two-tailed t-test.

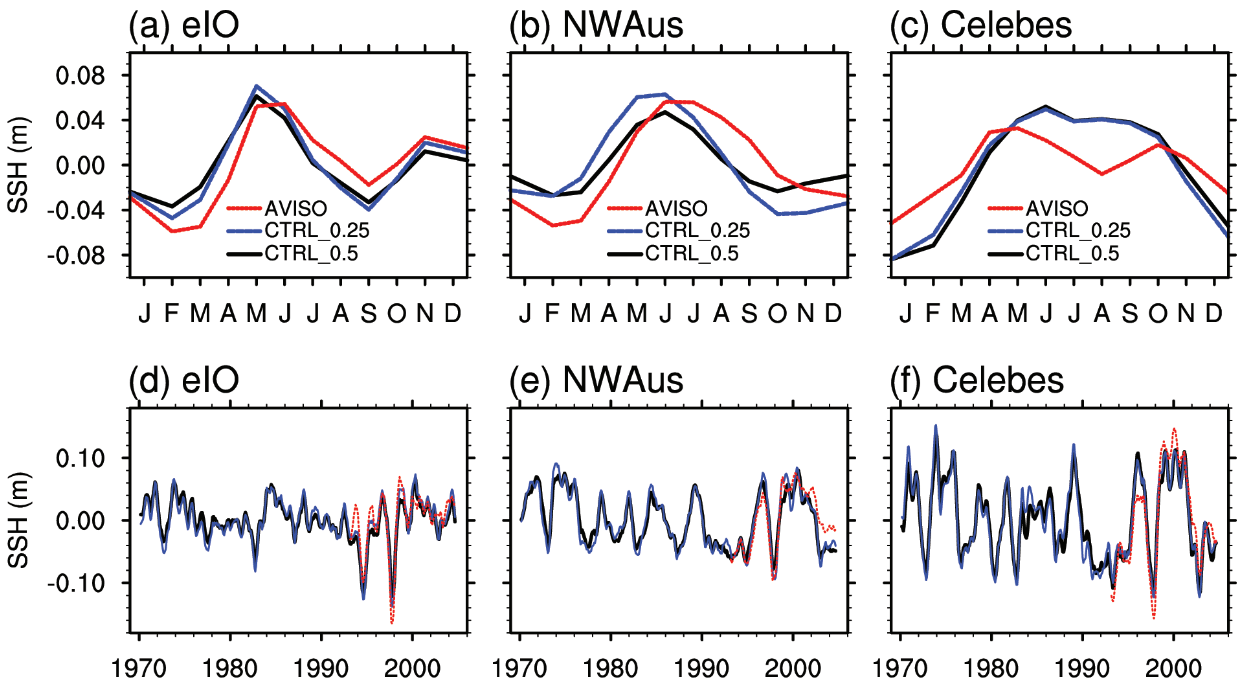

FIG. 10. Observed and model variability in SSH in key regions around the Maritime Continent: (a–c) Seasonal cycle of SSH and (d–f) anomalous SSH time-series for the three different regions indicated in Fig. 3. SSH based on control model simulations at (black) 0.5° and (blue) 0.25° horizontal resolution, as well as observed SSH from Aviso (red). With the exception of the observations (1993–2004), the analysis period covers 1970–2004.

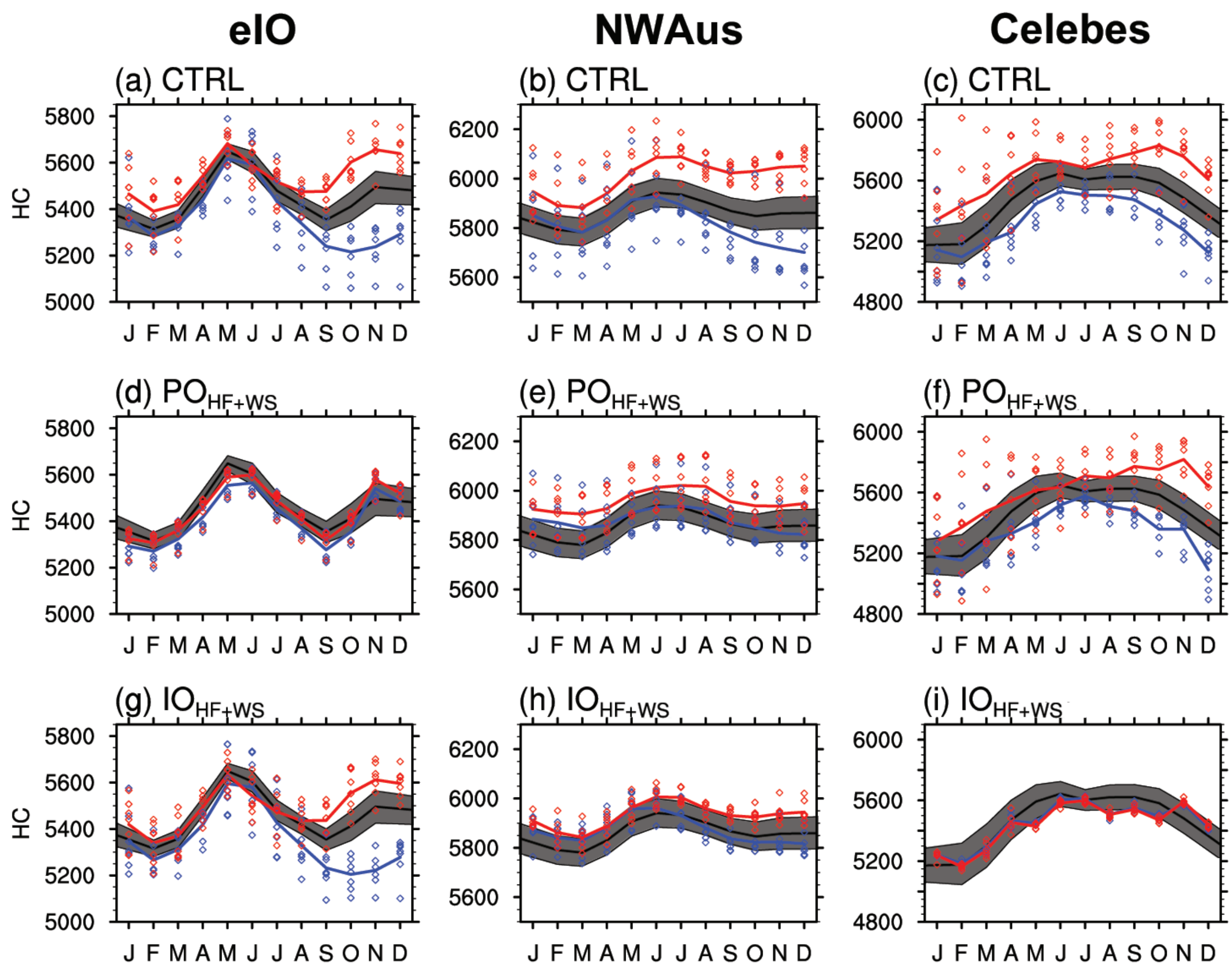

FIG. 11. Seasonal cycle in heat content during anomalous low and high heat content events in key regions: composite heat content for the three different regions indicated in Fig. 3 for (top) control, (middle) PO_{HF+WS}, and (bottom) IO_{HF+WS} experiments for the period 1970–2004. The black line reproduces the long-term seasonal cycle for all years, with the 90% confidence levels indicated by the gray shading. The red (blue) line represents the mean during high (low) heat content events in the eastern Indian Ocean, with individual years shown with red (blue) dots. Where the red (blue) line lies outside the gray shaded area, the values are significantly different from the long-term seasonal cycle in the control.

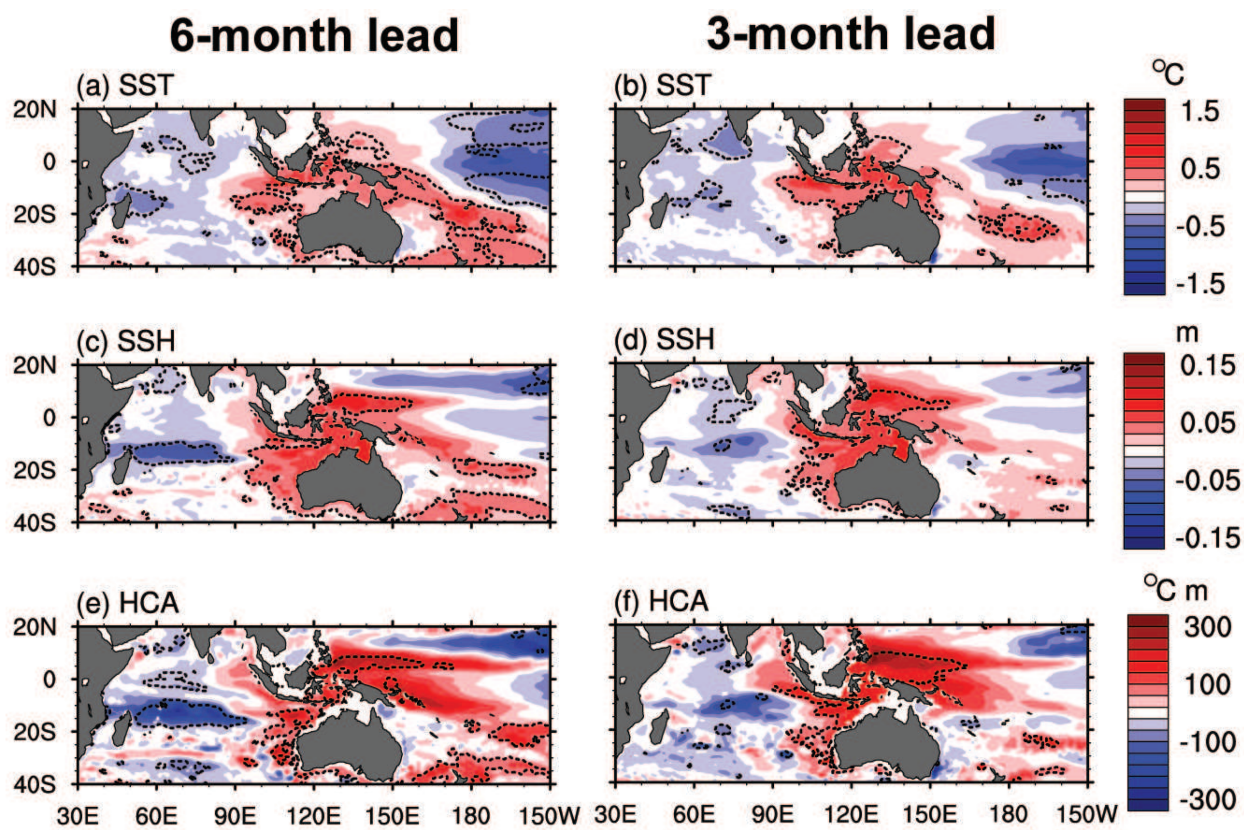

FIG. 12. Pacific predictor for Indian Ocean high heat content: composite anomalies of (a–b) SST (°C), (c–d) SSH (m) and (e–f) heat content (°C m) during September–November for years with high heat content anomalies in the Celebes Sea region at (left) 6-months and (right) 3-months lead in the control model simulation for the period 1970–2004.

List of Tables

Table 1. Summary of ORCA ocean model simulations used in the study, with interannual (I) or climatological (C) forcing of heat fluxes (HF) and wind stress (WS) indicated for the respective regions (see Fig. 2 for masks). The acronym used in the text is highlighted and the respective DRAKKAR name of the simulation provided for reference.

Acronym	**DRAKKAR name**	**Resolution**	**Global**		**Pacific Ocean**		**Indian Ocean**	
			HF	WS	HF	WS	HF	WS
CTRL	KAB109	0.5°	I	I	I	I	I	I
CTRL_0.25	K335	0.25°	I	I	I	I	I	I
CLM	KAB108	0.5°	C	C	C	C	C	C
CLM_0.25	K350	0.25°	C	C	C	C	C	C
$\mathbf{PO}_{HF+WS}$	KFS118	0.5°	C	C	I	I	C	C
$\mathbf{IO}_{HF+WS}$	KFS119	0.5°	C	C	C	C	I	I
$\mathbf{PO}_{HF}$ $\mathbf{IO}_{HF+WS}$	KFS115	0.5°	I	C	I	C	I	I
$\mathbf{PO}_{HF+WS}$ $\mathbf{IO}_{HF}$	KFS100	0.5°	I	C	I	I	I	C